

## EASI: An Air–Sea Interaction Buoy for High Winds

W. M. DRENNAN, H. C. GRABER, C. O. COLLINS III, A. HERRERA, H. POTTER,  
R. J. RAMOS, AND N. J. WILLIAMS

*Rosenstiel School of Marine and Atmospheric Science, University of Miami, Miami, Florida*

(Manuscript received 22 September 2013, in final form 2 March 2014)

### ABSTRACT

This paper describes the new Extreme Air–Sea Interaction (EASI) buoy designed to measure direct air–sea fluxes, as well as mean properties of the lower atmosphere, upper ocean, and surface waves in high wind and wave conditions. The design of the buoy and its associated deep-water mooring are discussed. The performance of EASI during its 2010 deployment off Taiwan, where three typhoons were encountered, is summarized.

### 1. Introduction

Over the past decade, there has been renewed interest in air–sea fluxes in the high wind regime. Here, we define as “high” those winds with speeds of over  $20 \text{ m s}^{-1}$ , corresponding roughly to Beaufort force numbers 9 and over. This regime has long been distinguished by mariners by the presence of breaking waves and high concentrations of sea spray in the marine atmospheric boundary layer. Scientifically, this regime is of interest, in that high wind fluxes play a controlling role in the development and maintenance of tropical cyclones. High winds also dominate the high-latitude regions, where poor knowledge of surface fluxes is a key limiting factor in our understanding of global budgets of heat and carbon, *inter alia* (Bourassa et al. 2013).

In strong wind conditions, the interface is dominated by breaking waves, entrained air, ejected droplets, and spume lifted or sheared off the crests of steep waves. The significance of wave breaking in affecting both sides of the interface has been demonstrated by laboratory studies and numerical models (Banner and Melville 1976; Reul et al. 1999; Belcher and Hunt 1998; Makin 1998) on the air side and by field measurements (e.g., Terray et al. 1996; Gemmrich and Farmer 2004) on the water side.

Fairall et al. (2009) recently summarized the air–sea exchange estimates from three field-based air–sea

interaction groups, representing tens of thousands of hours of data collected over the past 15 years. There is a remarkable consistency in the mean bulk relations of the three groups for wind speeds between 5 and  $15 \text{ m s}^{-1}$  (their Fig. 5): the mean drag coefficient increases roughly linearly with wind speed, while the bulk coefficients for latent and sensible heat (the Dalton and Stanton numbers, respectively) are constant. At higher wind speeds, the amount of data drops significantly with very few points, representing a few isolated events, at wind speeds above  $20 \text{ m s}^{-1}$ .

Several papers published in the last decade support a fundamental change in behavior of the bulk coefficients at higher wind speeds. Powell et al. (2003), estimating the drag coefficient using an extensive set of GPS dropsonde observations from many years of hurricane flights, found the drag coefficient to level off at high winds ( $>32 \text{ m s}^{-1}$ ), and then decrease for winds above  $40 \text{ m s}^{-1}$ . Donelan et al. (2004) in a controlled laboratory study found a leveling off of the drag coefficient at high winds, in their case over  $33 \text{ m s}^{-1}$ . Finally, the low-level aircraft data of French et al. (2007), collected in several hurricanes, indicated a flattening of the drag coefficient curve before  $30 \text{ m s}^{-1}$ .

Likewise, the Dalton number has been predicted to increase at higher wind speeds due to the effect of sea spray (Andreas 1992). While this has not been observed in field data to date (see, e.g., Drennan et al. 2007; Sahlée et al. 2012), it cannot be ruled out at higher winds, as per the model predictions of Bao et al. (2011).

The present dearth of high wind speed measurements is related both to the relative rarity of winds over

---

*Corresponding author address:* William M. Drennan, Rosenstiel School of Marine and Atmospheric Science, University of Miami, 4600 Rickenbacker Causeway, Miami, FL 33149-1098.  
E-mail: w.drennan@miami.edu

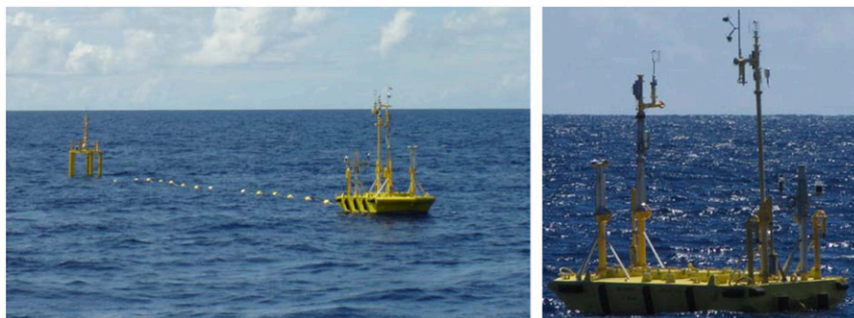


FIG. 1. (left) Photograph of EASI (foreground) and ASIS buoys taken shortly after deployment during ITOP. The 60-m surface tether connecting ASIS to EASI is clearly seen. (right) Close-up of EASI showing meteorological instruments. Bow is to the left.

$20 \text{ m s}^{-1}$  and to the lack of suitable platforms from which to make such measurements. Waves in the vicinity of coastal towers tend to be strongly modified by both shoaling and refraction in these conditions, while ship motion is greatly amplified in large breaking waves. The Air–Sea Interaction Spar (ASIS) buoy (Graber et al. 2000) has survived seas of over 7-m significant height,  $H_s$  (Knobles et al. 2008), but it is not designed for extended deployments in these conditions. Here, we define  $H_s$  as 4 times the standard deviation of surface elevation.

Recently, we designed and built a platform specifically for extended surface deployments in extreme wave environments. The platform would be capable of high-resolution measurements of direct (i.e., via eddy correlation) air–sea turbulent fluxes of momentum, sensible heat, latent heat and carbon dioxide, mean meteorology, surface waves, and mean upper-ocean characteristics. In designing the platform, three criteria were initially established. The first was the durability of the platform in high sea states. This includes the capability of unattended operation for one year, and survivability in a high wind, high sea-state environment. Following a survey of existing platforms, we decided to base the design of the new Extreme Air–Sea Interaction (EASI) buoy on that of the Navy Oceanographic Meteorological Automatic Device (NOMAD) buoy designed in the 1940s for navy use (Timpe and van de Voorde 1995). The 6-m NOMAD buoy is currently used by the U.S. National Data Buoy Center (NDBC) for most of its open-ocean deployments. The NOMAD is also used by the Canadian Marine Environmental Data Service (MEDS). The ship-hull-shaped NOMAD buoy (Fig. 1) has proven capabilities to survive the rough wintertime conditions of the North Pacific and North Atlantic.

The second criterion was minimal flow distortion. There has been considerable attention paid to the effects of flow distortion on meteorological measurements (e.g., Oost et al. 1994; Dupuis et al. 2003). Flow distortion

affects both the mean and turbulent components of the flow field, and can have a significant effect on direct (eddy correlation) turbulent fluxes, particularly that of momentum (Pedreros et al. 2003). This second criterion led to a redesign of the buoy superstructure from that used by NDBC and MEDS. Both these agencies include an array of solar panels mounted on a  $\sim 1$ -m mast on the forward deck. While this configuration allows for the use of rechargeable batteries, the flow distortion around the array was estimated to result in unacceptable errors in the turbulent flux measurements, which are not made on the NDBC or MEDS platforms. Hence, the solar panels were eliminated from the present design. This was also thought to reduce the risk of vandalism. We further discuss the power system of the EASI buoy below. The third criterion was the capability to safely deploy the buoy in rough seas. This last criterion was eventually dropped for practical reasons: no major “over the side” ship operations are possible in high sea states.

Two of the new EASI buoys were recently deployed off Taiwan as part of the Impact of Typhoons on the Ocean in the Pacific (ITOP) experiment. The seas east of Taiwan are known to be a particularly active region for tropical cyclone development (Pun et al. 2011). During ITOP three typhoons and one tropical storm passed over or near each of the buoys. Here, we describe the design of buoys, as well as their performance in sea states as high as 10-m significant wave height.

## 2. Research platform

As discussed above, the EASI buoy hull is that of the original NOMAD buoy, which has a ship-hull shape with dimensions 6 m long  $\times$  3 m wide  $\times$  3 m high. The EASI exterior hull and deck are made of a 13-mm-thick aluminum plate with an overall tare weight of 3900 kg. The interior contains four compartments separated by 10-mm-thick bulkheads. The bulkheads are fully

TABLE 1. Meteorological and oceanographic instruments installed on EASI-N (N) and EASI-S (S) during the ITOP campaign. Two CLASP units were also deployed on each EASI.

Sensor	No. of sensors deployed	Condition on recovery
Gill 1012R2A sonic anemometer	N(2); S(1)	1 failed; 1 OK; 1 noisy
Gill WindMaster Pro sonic anemometer	S(1)	Failed
K-Gill anemometer	N;S	1 OK; 1 lost blade
R. M. Young Marine Wind Monitor	N;S	1 OK; 1 bad bearings
Rotronic MP101A-T7 (temp/RH)	N(2); S(2)	Some suffered water intrusion
Setra 278 barometer	N(2); S(2)	OK
LI-COR LI-7500 infrared gas analyser	N(1*); S(1)	H <sub>2</sub> O OK
LI-COR LI-7200 infrared gas analyser	S(1)	Unit seized up
Eppley PSP pyranometer	N(2); S(2)	OK
Eppley PIR radiometer	N(2); S(1)	OK
Campbell 107-L thermistor (hull)	N(2); S(2)	OK
Wadar TL-HA thermistor (air side)	N(2); S(2)	OK
Brancker TR-1050, TDR-2050, TDO-2050, TR-1000, Hygrun Seamon thermistors	Many on mooring lines	Several failed near surface, likely due to vibration of wire rope

\* An additional modified LI-7500 was deployed on EASI-N.

watertight with the exception of two 100-mm-diameter openings near the top of each bulkhead. These channels, used to pass cables between compartments, are effectively sealed by potting the cables in Roxtec frames and sealing modules. A false floor in each compartment allows for the addition of lead ballast to ensure proper trim of the buoy. Six 225-kg lead ingots were also bolted onto the keel of EASI.

The compartments are used for the electronics, data, and power systems of the buoys. Given the extreme nature of the expected environmental conditions, two fully isolated and redundant power/data/sensor systems were used on each buoy. On each buoy, one data acquisition system was the custom personal computer (PC)-based system developed for use on the University of Miami ASIS buoy. The other was a Campbell Scientific CR3000 micrologger. Summary data, including position, were transmitted back to shore in near-real time over both ARGOS and Iridium satellites. With the decision to move away from rechargeable batteries, several alternative power arrangements were considered. Cegasa air alkaline batteries were tested, but they delivered only about one-third of the expected power, likely due to limited air exchange. Although each pair of compartments was vented to the exterior with a 0.7-m-high, 50-mm-diameter inverse-U-shaped vent fitted with a ball valve, air exchange with the exterior was passive, relying on pumping from the moving buoy. The final decision was made to use custom packs of D-cell alkaline batteries wired to produce a 15-V output. The packs were installed in custom tray units mounted in each compartment.

To dispense with (or minimize) guy wires and exposed cables, the EASI masts were made from flanged pipe segments. The upper two-thirds portion of each tall mast was hinged to the lower one-third portion, allowing the

upper portion to be supported horizontally on the deck for setup. This arrangement allows instruments to be worked on from the deck fairly easily with the masts down. It also permits deployment of EASI through a large A-frame, again with masts down. The total height of the tall masts was 3.5 m above the deck. The highest instruments, sonic anemometers mounted at the top of the tall masts, were 5.4 m above mean sea level. Cables were strung inside the pipe masts, and passed directly into the interior through holes in the deck located within flanged pipe base segments welded onto the deck. Rubber gaskets were used between mating flanges, and Roxtecs located below the deck ensured a water-tight seal in the event of a mast failure.

EASI uses two fully duplicate mast pairs, one fore and one aft, with each pair connected to independent power and data systems. The instrument suite is summarized in Table 1. The tall mast of each pair was mainly dedicated to turbulence measurements, the other to mean parameters. The turbulence sensor suite consisted of a Gill 1012-R2A sonic anemometer (or in one case, a Gill WindMaster), a LI-COR infrared gas analyzer (IRGA), and a Compact Lightweight Aerosol Spectrometer Probe (CLASP; Norris et al. 2008), with a Rotronic MP101A-T7 temperature and relative humidity (RH) sensor mounted nearby. One turbulence suite on each buoy included a standard open-path LI-COR LI-7500. Given previous experience of poor sensor performance in saturated environments (cf. Sahlée et al. 2012), the other suite on each buoy included a closed-path IRGA. On one buoy this was a LI-7200; on the other a LI-7500 was modified for closed-path operation as described in Sahlée and Drennan (2009).

The Rotronic MP101A-T7 temperature and relative humidity sensors were mounted on R. M. Young radiation

shields. Several of the shields were modified by sealing adjacent plates with room-temperature vulcanizing silicone (RTV) so as to prevent spray from wetting the sensor in high winds. All plates on the windward side of the shield were sealed. While this significantly reduced airflow to the sensor, leaving measurements useless at low winds, it was thought the large vertical motions of the platform at high winds (waves) would provide sufficient ventilation while eliminating the sea spray. Sensors in standard (unmodified) shields would be used in lower wind conditions.

On each buoy one turbulence suite was supplemented with a K-Gill anemometer. The K-Gill is a vintage 1980s sensor that measures two components of the wind in a vertical plane using two Gill propellers with carbon-fiber blades mounted at  $\pm 45^\circ$  from the horizontal (Katsaros et al. 1993). The K-Gill was deployed here out of concerns for the reliability of sonic anemometers in a rain- or spray-dominated environment (see Fig. 9 of Eckman et al. 2007). The turbulence suite was designed to measure the eddy correlation fluxes of momentum, sensible heat (via the sonic temperature signal; see Drennan and Shay 2006), latent heat, carbon dioxide, and aerosols.

The sensor suite on the “mean” mast of each pair consisted of an R. M. Young Marine Wind Monitor (rear mast only), a Setra model 278 barometer, an Eppley Precision Spectral Pyranometer (PSP), and an Eppley Precision Infrared Radiometer (PIR). On each buoy, one of the Setra barometers directly sensed the exterior pressure with an aft-facing port. To alleviate concerns of possible high wind Bernoulli effects on this sensor, the second barometer measured the EASI interior pressure, relying on the EASI vents to achieve equilibrium with the exterior. The measurements from the two systems generally differed by less than 0.4 hPa—well within the limits of calibration. Finally, an arm on the rear mean mast on each buoy held a Carmanah M704 marine lantern.

Each EASI buoy was equipped with two full sets of strapped-down motion sensors, one in the bow compartment and the other in the stern, and each associated with one of the two acquisition systems. Each motion pack consisted of a triaxial linear accelerometer (Columbia Research Laboratories SA307-HPTX), three orthogonally mounted rate gyros (Systron Donner model QRS110050 or SDG1000), and a compass (Precision Navigation TCM-2). As described in Graber et al. (2000), the rotational motions are reconstructed using a complementary filtering routine combining the rate gyros for high frequencies and the linear accelerometers or compass for low frequencies. The motion signals are used to correct the measured anemometer signals to a stationary reference frame [see Graber et al. (2000) and Drennan et al. (2003) for details], as well as for assessing the performance of the

buoys (see below). In addition the doubly integrated vertical buoy acceleration provides an estimate of surface elevation,  $\eta$ . In practice, this involves calculating

$$\eta = \iint (-a_1 \sin\theta + a_2 \cos\theta \sin\phi + a_3 \cos\theta \cos\phi - g) dt dt, \quad (1)$$

where  $\mathbf{a}$  = (surge, sway, heave) are the linear accelerations from the strapped-down accelerometer,  $\theta$  is pitch,  $\phi$  is roll, and  $g$  is gravitational acceleration. Clearly the hull of EASI acts as low-pass filter on  $\eta$ , filtering scales less than the 6-m buoy length.

For water-side measurements, EASI is fitted with a 24-cm-diameter flanged well protruding through the hull and deck, which is designed to hold a downward-looking acoustic Doppler current profiler (ADCP). While an ADCP was not deployed from EASI during ITOP, several thermistors were attached to the well to measure water temperature near the surface (1 m below the mean surface). A hull-mounted sensor was also deployed. In addition, a dozen thermistors of various designs (Hugrun Seamon mini; Wadar TL; Brancker TR-1000; RBR TR-1050, TDO-2050, and TDR-2050) were deployed in the top 200 m along the mooring line, the design of which is discussed below. Some of the thermistors included pressure sensors, which allowed for the depth to be calculated; others included dissolved oxygen. All thermistors were cross calibrated in controlled thermal baths at the Rosenstiel School of Marine and Atmospheric Science (RSMAS) prior to the experiment.

The mooring design is critical to the durability of any surface mooring, especially in high sea states. Here, we used an inverse-catenary-style mooring designed for full ocean depth. The mooring consisted of (from the top): 27 m of 1 1/2-in. (4 cm) galvanized stud link chain attached to (and isolated from) the stainless steel EASI yoke and serving primarily as ballast (764 kg); 2000 m of jacketed wire rope (1.3-cm outer diameter); 1850 m of 2.5-cm-diameter braided nylon rope; 3125 m of 2.8-cm-diameter Sampson Ultra Blue eight-braid polypropylene rope (positively buoyant); 52 Benthos 2040-17V glass flotation spheres mounted on 9.5-cm galvanized chain; dual ORE model 8242XS acoustic releases; 5 m of 9.5-cm galvanized chain; a 30-m section of 2.5-cm nylon (acting as a shock absorber for the anchor launch); 5 m of 9.5-cm galvanized chain; and terminating in a 3100-kg anchor. The total mooring length of 7050 m, designed for a depth of 5600 m, allowed for a scope of 1.26.

### 3. ITOP experiment

The ITOP experiment took place during August–November 2010 in the Philippine Sea, east of Taiwan.

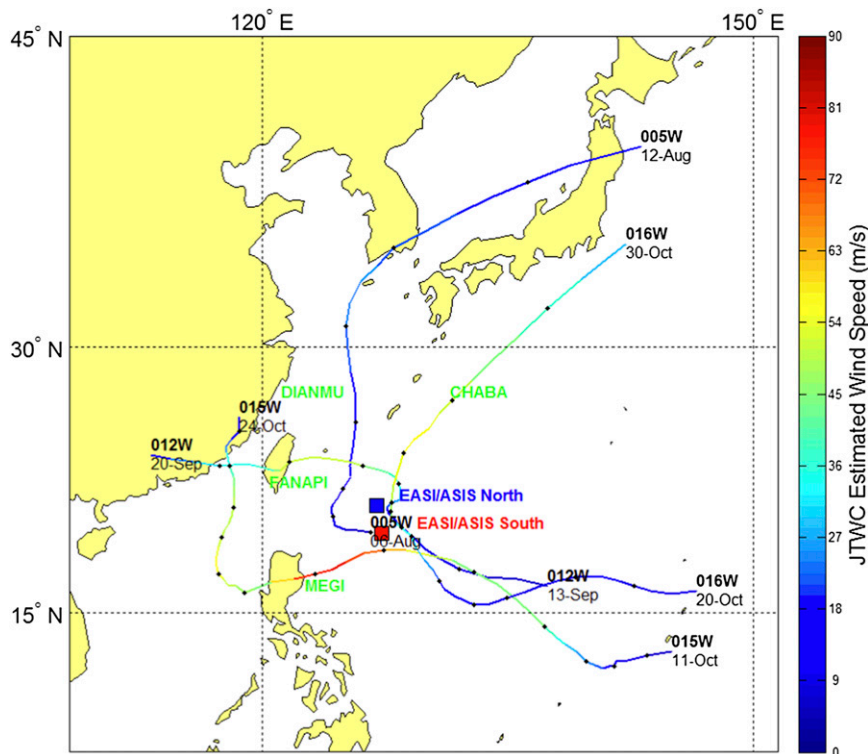


FIG. 2. Positions of EASI-N and EASI-S moorings during 2010 ITOP experiment. The tracks of Tropical Storm Dianmu (005W, 5–12 Aug), Typhoon Fanapi (012W, 13–20 Sep), Super Typhoon Megi (015W, 11–24 Oct), and Typhoon Chaba (016W, 20–30 October) are also shown. The storm-track color indicates wind speed as estimated from the Joint Typhoon Warning Center, while the dots indicate 0000 UTC positions.

The purpose of the experiment, as per the name, is to investigate the impact of tropical cyclones on the ocean, including the feedbacks between the ocean, atmosphere, and surface waves. The overall experiment included two aircraft [a U.S. Air Force C-130 out of Guam, and the Taiwanese Dropwind Observations for Typhoon Surveillance near the Taiwan Region (DOTSTAR) Astra], several ships [the Research Vessel (R/V) *Roger Revelle* and the R/V *Ocean Researchers 1–3*], a variety of floats and buoys, as well as significant satellite and modeling components. Here, we focus on the two EASI buoys deployed in early August from the R/V *Roger Revelle*. The role of the EASI buoy deployment within ITOP was to measure mean lower-atmospheric and upper-oceanic parameters, along with surface waves and air–sea fluxes of momentum and energy.

The two EASI buoys, designated North and South (EASI-N and EASI-S, respectively), were deployed at 21.2°N, 126.8°E (5450-m depth) and 19.6°N, 127.3°E (5500 m), respectively (see Fig. 2). The buoys were deployed on 6 and 4 August [year days (YD) 218 and 216], respectively, with sufficient power and disk capacity for

an expected 100-day duration. All data on the custom data acquisition system were sampled at 20 Hz. Because of storage limitations, turbulence and wave and motion data on the Campbell system were recorded at 5 Hz; other Campbell sensors were recorded every 60 s. Data were subsequently analyzed in 30-min blocks. Because of heavy weather encountered during the scheduled recovery cruise (which coincided with Typhoon Chaba, see below), the buoys were not recovered until March 2011. Data collection on the buoys ended on 13 December and 22 November, respectively. Below we use the term *deployment period* to refer to the time of data collection.

Attached to each EASI buoy with a 60-m surface tether was an ASIS buoy. The primary function of the ASIS buoys was to measure surface waves, using an array of capacitance wave wires. See Petterson et al. (2003) for a description of the array and subsequent processing. The outer perimeter wires were extended 76 cm over previous ASIS deployments to reduce the overtopping of wave staffs during high wave conditions. While this reduced the problem, some wave overtopping did occur. Such cases were corrected on a wave-by-wave

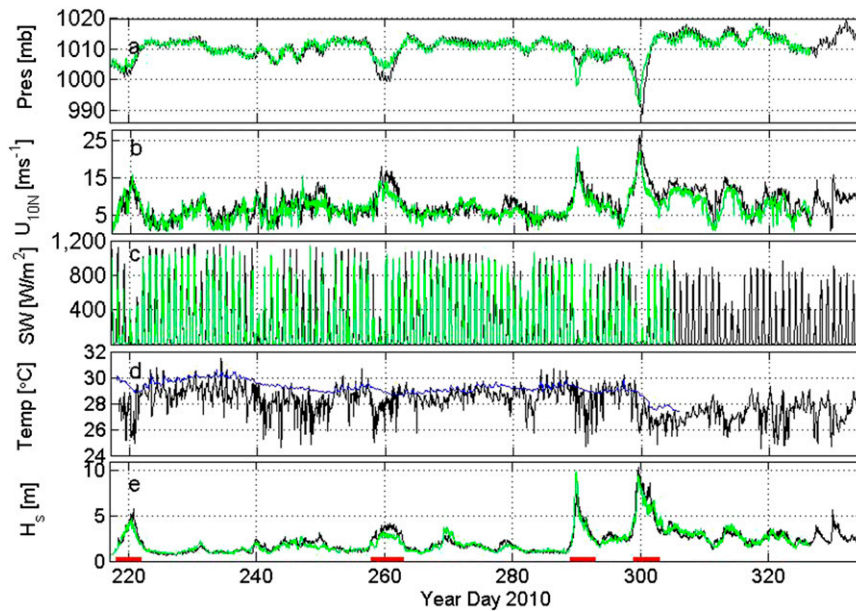


FIG. 3. Time series data from EASI-N (black, blue) and EASI-S (green) during ITOP experiment. Shown are (a) barometric pressure, (b) 10-m neutral wind speed, (c) downwelling SW, (d) atmospheric and near-surface water (blue) temperatures, and (e) significant wave height. The near passages of Tropical Storm Dianmu (YD 218–221), Typhoons Fanapi (YD 258–262) and Chaba (YD 299–301), and Super Typhoon Megi (YD 289–290) are indicated in (e).

basis using the cubic spline routine described in Sahlée et al. (2012). ASIS data were sampled at 20 Hz and analyzed in blocks of 30 min.

Conditions during ITOP are plotted in Fig. 3. The passages of Tropical Storm Dianmu (year days 218–221), Typhoons Fanapi (258–262) and Chaba (299–301), and Super Typhoon Megi (289–290), indicated in Fig. 3e, are clearly evident in the atmospheric pressure (Fig. 3a), wind speed (Fig. 3b), and significant wave height (Fig. 3e). The four storm tracks are shown in Fig. 2. Here, the measured 5.4-m wind speeds are converted to 10-m neutral equivalents  $U_{10N}$  assuming logarithmic neutral mean wind profiles and the stability relations  $\Phi_u$  of Donelan (1990):

$$\frac{U_z - U_0}{u_*} = \frac{1}{\kappa} \left[ \log\left(\frac{z}{z_o}\right) - \Phi_u\left(\frac{z}{L}\right) \right] \quad (2)$$

The calculation of the Obukhov length  $L$  in the stability relations uses measured friction velocity ( $u_*$ , see below) and the bulk sensible and latent heat flux relations of Smith (1980). Here,  $\kappa = 0.4$  is the von Kármán constant, and  $z_o$  is the surface roughness length; see Drennan (2006) for details. Maximum 30-min winds at the buoys reached  $26 \text{ m s}^{-1}$ , and maximum significant wave heights over 10 m were recorded.

#### 4. Performance of EASI during ITOP

The performance of EASI as a platform will be evaluated on several aspects. At the most basic level, the mechanical system components survived the high winds and sea states associated with several typhoons: all masts remained upright and there was no evidence of any water leakage in the interior compartments. The only significant mechanical failures occurred at the tethers linking the EASI and ASIS buoys. Both failed during the high wave conditions of either Typhoons Fanapi (North mooring, YD 260.7) or Megi (South mooring, YD 289.7). Just before the break on EASI North, surge accelerations on ASIS reached  $0.5g$  due to the snap loading of the tether as EASI crested a wave and accelerated down the rear face. The ASIS buoys are not an integral part of the EASI design, but it is clear that if ASIS and EASI are to be deployed together in the future, a shock-absorbing tether must be used. The two ASIS buoys, each equipped with multiple satellite beacons, were recovered by the R/V *Revelle* on YD 287 (ASIS-N) and YD 295 (ASIS-S).

The standard deviation of pitch and roll of EASI as a function of wind speed are plotted in Figs. 4a and 4b, respectively. Quadratic fits to the data explain 78% and 76% of the variance, respectively. It is clear that while EASI has considerable motion in both pitch and roll at

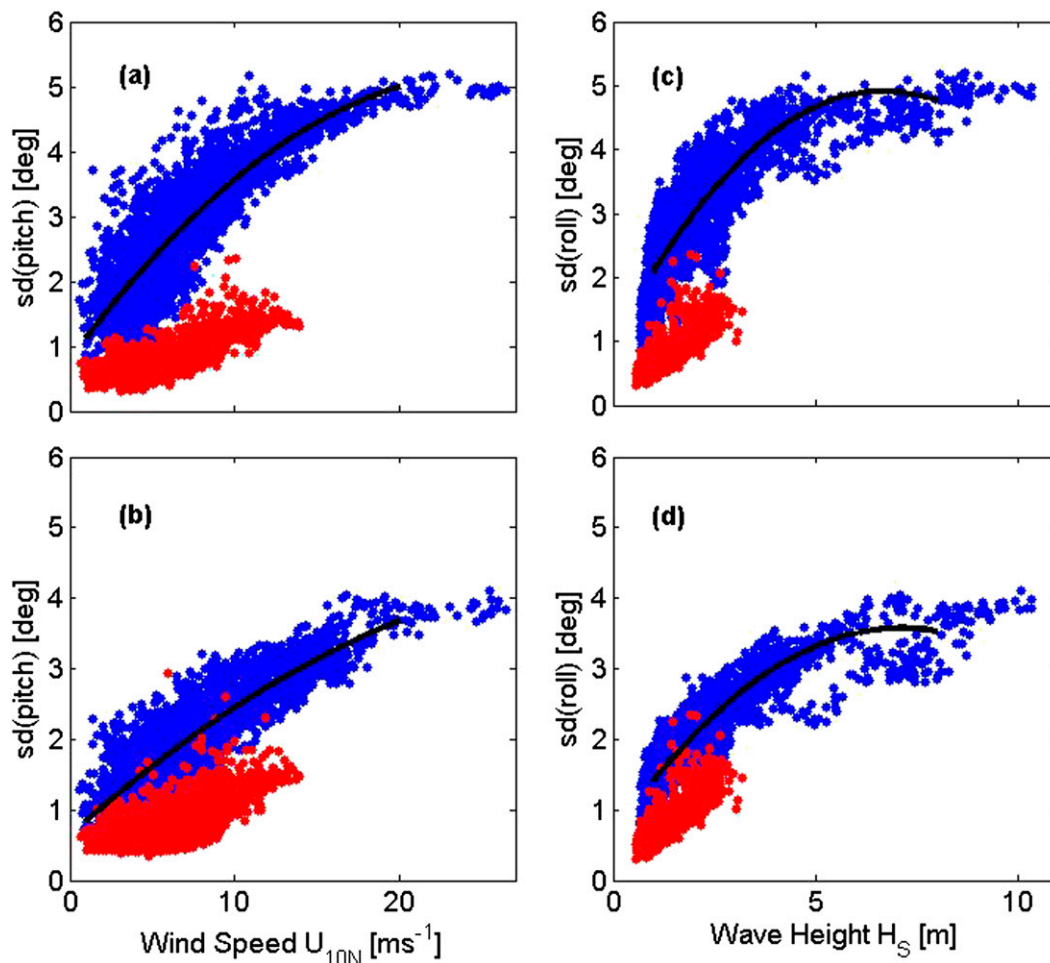


FIG. 4. Standard deviations of 30 min of (a) pitch and (b) roll vs 10-m neutral wind speed measured on EASI-N during ITOP. Motion data are from EASI (blue) and ASIS (red), the latter shown only for the period when ASIS and EASI were attached. The curves represent the best quadratic fit to the EASI data. (c),(d) As in (a) and (b), but plotted against significant wave height.

low winds (very evident when on board), the standard deviation of pitch rarely exceeded  $5^\circ$  (only during 12 runs, with a maximum of  $5.2^\circ$ ), while that of roll exceeded  $4^\circ$  during only 3 runs (maximum  $4.1^\circ$ ). Significant wave height does not explain significantly more variance in  $\text{std}(\text{pitch})$  or  $\text{std}(\text{roll})$  (Figs. 4c and 4d), and the quadratic fits are questionable at high wave heights. Equivalent data from ASIS-N are also plotted for the period when ASIS was attached to EASI. The motion of ASIS in pitch and roll is roughly one-third that of EASI, consistent with the numbers reported by Graber et al. (2000). ASIS was designed specifically for stability in pitch and roll, while EASI is expected to more closely follow the surface.

In Fig. 5, we plot time series of the main motion components (heave, surge, sway, pitch, and roll), as well as the surface elevation. The 100-s time series, from

Typhoon Chaba (YD 300, after 0610 UTC), are some of the roughest conditions experienced during ITOP. During the 30-min period of the run,  $U_{5.4} = 20.4 \text{ m s}^{-1}$  and  $H_s = 8 \text{ m}$ . Using (2), the 10-m neutral wind speed is  $U_{10N} = 21.7 \text{ m s}^{-1}$ . Here, the standard deviations of pitch and roll are  $5.17^\circ$  and  $3.86^\circ$ , respectively. Maximum instantaneous pitch and roll angles of  $27.9^\circ$  and  $24.8^\circ$  were recorded, both during the passage of a single 15-m wave. The trough-to-trough wavelength was  $\lambda = 202 \text{ m}$ , giving  $ak = a(2\pi/\lambda) = 0.23$ , consistent with the recorded instantaneous tilt angles. Here  $a$  is half the peak-to-trough height. These pitch and roll values were close to the maximum recorded during the experiment. Maximum horizontal acceleration during the wave passage reached  $8.27 \text{ m s}^{-2}$ , or  $0.86 \text{ g}$ , well in excess of the limits proposed by Longuet-Higgins (1985). It is therefore likely that the wave was breaking.

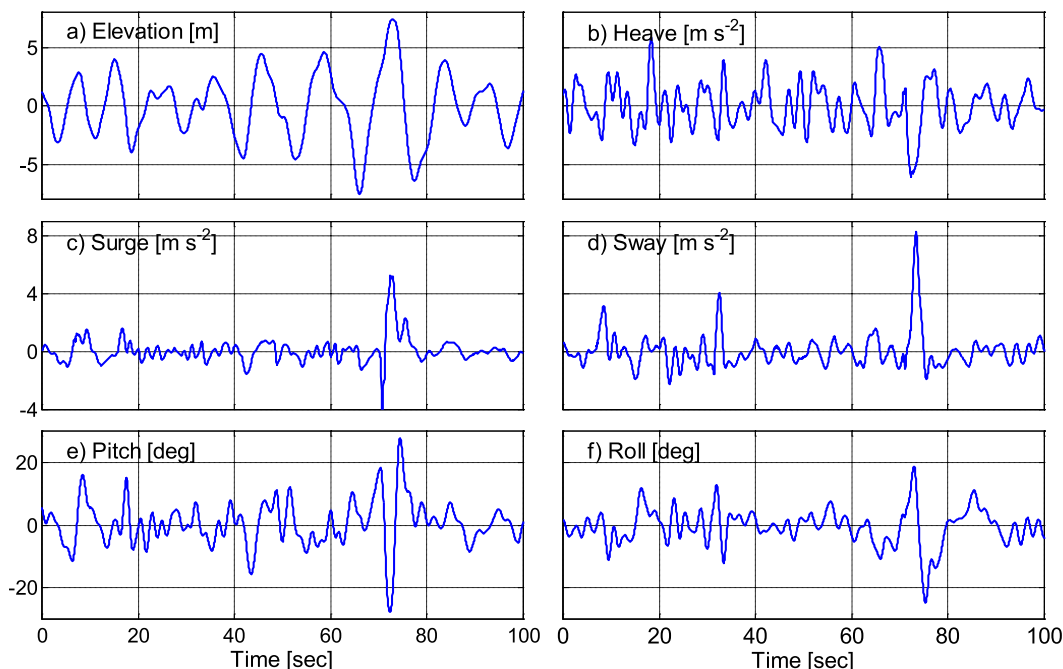


FIG. 5. Time series of (a) surface elevation, (b) heave with  $g$  removed, (c) surge, (d) sway, (e) pitch, and (f) roll measured from the motion package on EASI-N for the 100 s starting at 0610 UTC 27 Oct 2010 (YD 300.26) during Typhoon Chaba. The mean wind speed for the 30-min run was  $20.4 \text{ m s}^{-1}$ , and the mean significant wave height was 8 m.

As described in Edson et al. (1998), motion correction algorithms including that used here (which is based on Anctil et al. 1994) employ a small angle assumption in deriving the rotation matrix used to correct the instantaneous angle of the platform. In practice this involves the assumption of separation of variables, so that the rotation matrix  $\mathbf{T}(\theta, \phi, \Psi)$ , where  $\Psi$  is yaw, can be written as the product of three independent rotations:  $\mathbf{T}(\theta, \phi, \Psi) = T_1(\theta) T_2(\phi) T_3(\Psi)$ . Here, higher-order terms ( $\theta^2$ ,  $\phi^2$ ,  $\theta\phi$ , etc.) are assumed to be negligible, and the order of the multiplication is arbitrary. As a test of the assumption, we calculate  $T_{ijk}$  for all six possible orders of multiplication, and calculate the variability among the  $T_{ijk}$ . The relationship between the maximum error in  $T_{ijk}$  (among the nine terms, compared to the average  $T$ ) and the rotation angle (assuming equal pitch, roll, and yaw angles) is quadratic in rotation angle. For a rotation angle of  $10^\circ$ , the error is under 2%, validating Edson et al.'s original assumption of a  $10^\circ$  limit in rotation angles. For a rotation angle of  $20^\circ$  ( $30^\circ$ ), the error reaches 8% (20%). Clearly, for some of the platform tilt angles experienced here, the assumption is no longer valid. However, the error analysis above assumes equal pitch, roll, and yaw. In fact, when pitch angles were high, the corresponding roll angles were near zero ( $0.2^\circ \pm 6.4^\circ$ , showing two standard deviations). If the error analysis is repeated for the

steepest recorded pitch angle of  $28^\circ$  and roll and yaw angles of  $6.6^\circ$ , then the rotation angle error is 5.7%, within the small angle assumption. Again, this is “worst case” during ITOP; typical errors are much smaller.

An additional consequence of platform tilt is to reduce the effective instrument heights from the nominal values. For this extreme run, 63% of all points had height corrections of less than 1%, while only 1.6% had corrections greater than 5%. The net effect is a mean reduction of measurement height by 1.0%. Mahrt et al. (2005) investigated the effect of nonconstant measurement heights on mean wind speed using the logarithmic mean wind profile [Eq. (2)]. Here, we follow their analysis using the instantaneous heights  $5.4\cos(\theta)\cos(\phi)$ , (where 5.4 m is the height of the anemometer in still conditions) and the measured friction velocity  $u_* = 0.86 \text{ m s}^{-1}$  for the run. The net effect of tilt in this extreme case is a reduction of measured wind speed by order 0.1%.

In assessing the performance of the buoy, it is instructive to compare the response of the buoy to the forcing of the surface. Here, we take the ASIS measurement of surface elevation, which has been validated by Petterson et al. (2003), as the true  $\eta$  and compare it with the EASI estimate derived from the integrated vertical displacement [Eq. (1)]. The 60-m offset between ASIS and EASI makes it difficult to interpret the phase

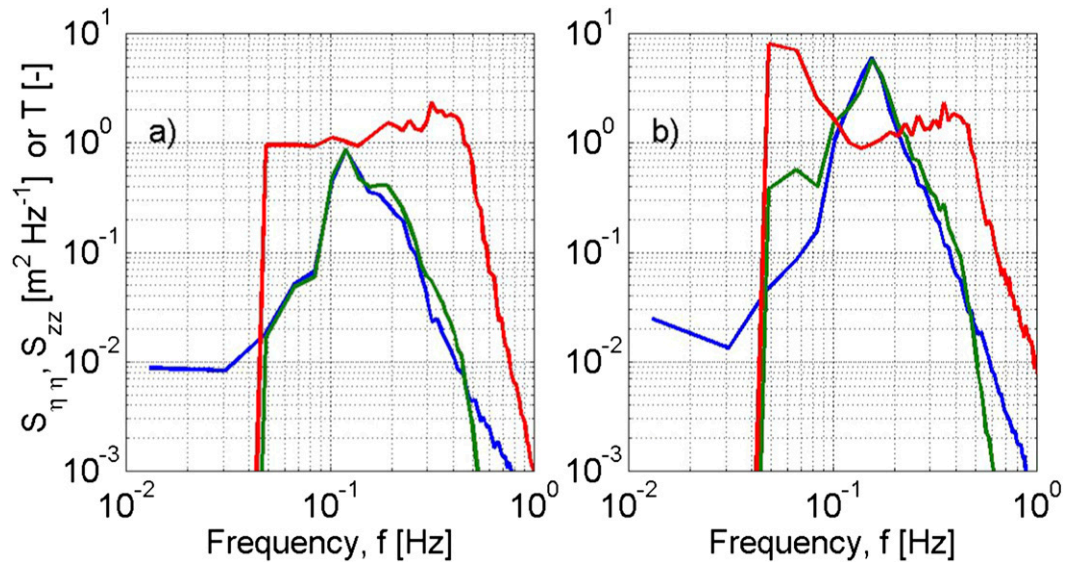


FIG. 6. Spectra of surface elevation from ASIS ( $S_{\eta\eta}$ , blue) and EASI ( $S_{zz}$ , green) along with transfer function  $T = S_{zz}/S_{\eta\eta}$  (red). Data are from EASI-N during two 4.5-h periods, starting at (a) 1759 UTC 10 Sep 2010 (YD 253.75;  $H_s = 1.12$  m,  $U_{10N} = 4.0$  m s $^{-1}$ ) and (b) 0145 UTC 16 Sep 2010 (YD 259.07;  $H_s = 2.81$  m,  $U_{10N} = 15.5$  m s $^{-1}$ ).

lag between forcing and response. We therefore consider here only the magnitude of the transfer function defined as  $T = S_{zz}/S_{\eta\eta}$ , where  $S$  represents the frequency spectrum,  $z$  is the vertical displacement of EASI (response), and  $\eta$  is the actual surface elevation (forcing). The transfer function plotted in Fig. 6a, based on 4.5 h of data starting on YD 253.75, is typical of light to moderate sea states. The term  $T$  is seen to be near unity in the vicinity of the wave energy peak (0.11 Hz), increasing to roughly 2 by 0.4 Hz, before decreasing rapidly as the smaller scales are cut off due to the 6-m length of the EASI hull. Note that the frequency of 0.4 Hz corresponds to  $\lambda = 10$  m. Surface elevation and EASI response spectra, and the heave transfer function, during the passage of Typhoon Fanapi, are shown in Fig. 6b. The transfer function  $T$  during these strongly forced conditions ( $U_{10N} = 15.5$  m s $^{-1}$ ;  $H_s = 2.81$  m) is largely similar to that during more moderate sea states, except at low frequencies when  $T$  reaches 8 around  $f = 0.06$  Hz (as opposed to near unity in moderate sea states). It is not clear whether this can be attributed to mooring dynamics, but since the associated heave energies are an order of magnitude below those of the peak, the effects are small. The surface tether linking ASIS and EASI broke just prior to the collection of these data, making this the last transfer function to be calculated. The 0.4-Hz natural frequency of the heave transfer function is consistent with that reported by Timpe and van de Voorde (1995) for previous NOMAD configurations. Their response amplitude operator (RAO, not defined but presumably the square root of our  $T$ )

reached a peak of 1.3 at the natural frequency, about 10% lower than our calculations. Their RAO reached a minimum of 0.7 around 0.33 Hz, a behavior not seen in the present data.

Timpe and van de Voorde (1995) also report an RAO for pitch that we are not able to estimate from the present data. Their pitch RAO has an amplitude near 1.15 in the range of wave frequencies 0.1–0.2 Hz, and it increases to 2.5 at the natural frequency of 0.38 Hz before dropping off.

### 5. Discussion and conclusions

The survival of EASI through a series of typhoons, with significant wave heights in excess of 10 m, gives confidence regarding the basic design of both the buoy and mooring. Ultimately, the success of the platform depends of the quality of the data recorded. Here, we assess the overall quality of several key meteorological and wave parameters, leaving to other papers a full description and discussion of these datasets.

The use of EASI accelerations to estimate wave height is predicated on the ability of EASI to follow the surface. The transfer function between buoy heave and surface elevation being near unity in the energy containing part of the spectrum (Fig. 6) confirms EASI does indeed follow the surface, at least in the vicinity of the peak. A comparison of significant wave heights measured from ASIS and EASI is given in Fig. 7. The maximum likelihood linear regression gives  $H_s$ -EASI = 0.96  $H_s$ -ASIS + 0.08 ( $r^2 = 0.974$ ; 5162 points), which is

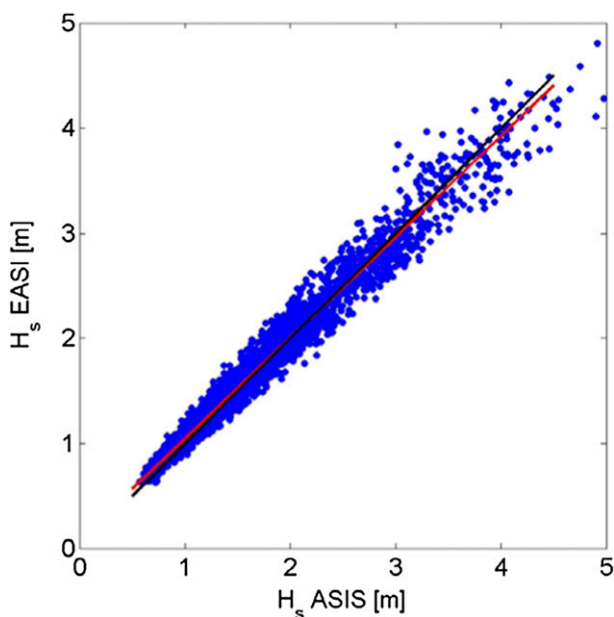


FIG. 7. Significant wave height by ASIS vs that measured by EASI while the two buoys were tethered together. The black line indicates a 1:1 curve. The red line is the best linear fit ( $H_s\text{-EASI} = 0.96 H_s\text{-ASIS} + 0.08$ ).

very close to the 1:1 line. Here, and in Fig. 7, all data from both North and South moorings when EASI and ASIS were tethered together are included. A more thorough discussion of the EASI wave measurements is given in Collins et al. (2013, manuscript submitted to *J. Atmos. Oceanic Technol.*).

Many individual meteorological sensors failed during the deployment, supporting the decision to use multiple redundant sensors on EASI. In particular, two sonic anemometers (an R2A and the WindMaster) failed during or following typhoon events, likely due to moisture (spray or rain) ingress into the electronics. Bearings failed on one of the Marine Wind Monitors, and one of the K-Gill anemometers lost a propeller blade. While Eckman et al. (2007) observed significant degradation of the sonic anemometer measurements during heavy rain events (droplet volumes in the acoustic path were large enough to affect the speed of sound), spray/rain effects during ITOP were limited to isolated spikes. These were readily identified from the sonic speed of sound channel, relatively rare (around 20 isolated events per 36 000 samples in a 30-min record at the highest winds observed), and easily corrected with interpolation. Wind data from multiple sensors compared favorably (not shown here), giving confidence in the individual measurements.

Turbulent components of the wind vector, after correction for platform motion (see Anttil et al. 1994), were

used to calculate the stress,  $\tau = \rho(-\overline{u'w'}\mathbf{i} - \overline{v'w'}\mathbf{j})$ , and friction velocity,  $u_* = (|\tau|/\rho)^{1/2}$ . Here,  $u'$ ,  $v'$ , and  $w'$  are the turbulent fluctuations of the horizontal mean wind, horizontal crosswind, and vertical wind components, respectively; and  $\rho$  is the mean air density. In Fig. 8 we plot the wind components  $u$  and  $w$ , both as measured and motion corrected, along with surface elevation, for the same 100-s segment as shown in Fig. 5. These are some of the roughest conditions experienced during the ITOP deployment and include the highest wave (15 m peak to trough) in the 30-min run. In Fig. 8d, we plot the  $uw$ -cospectrum, essentially the spectral representation of  $\overline{u'w'}$ , calculated with as-measured and motion-corrected velocity components. The motion-corrected spectrum is closer in shape to the classic universal spectrum of Miyake et al. (1970), albeit with a shift toward higher frequencies. Zhang (2010) also noted a blue shift in velocity spectra (larger than that seen here) for his aircraft data in several hurricanes. A detailed analysis of the momentum fluxes, including the influence of the wave field, is presented separately (Potter et al. 2014, manuscript submitted to *J. Atmos. Sci.*). Unfortunately, a comparison of the EASI winds and turbulence with those measured on ASIS is not possible, as the anemometer on ASIS failed during the deployment.

Downwelling shortwave (SW) radiation from both buoys is shown in Fig. 3c. To reduce flow distortion effects on the wind measurements, the radiometers are placed on shorter masts, below the level of the anemometers. This has the clear trade-off that the radiometers will at times be shaded by the taller masts. This was accounted for by placing the two pairs of radiometers (PSP + PIR) on the opposite corners of EASI, and using the higher PSP values of the two. Katsaros and Devault (1986) and MacWhorter and Weller (1991) present thorough discussions of the errors associated with making SW radiation measurements from buoys. Errors arise due to both the mean tilt and the wave-induced rocking of the pyranometer. Although all sensors (including the radiometers) were leveled on the deck prior to deployment, the accelerometers on board EASI-North indicate a mean of 30-min mean pitch angles, each calculated as  $\text{asin}(\overline{a_1}/g)$ , of  $4.72^\circ \pm 0.01^\circ$ , indicating two standard errors. The maximum and minimum 30-min mean pitch angles on EASI-North during ITOP were  $5.9^\circ$  and  $3.3^\circ$ , respectively. The mean 30-min roll angles were near zero, with a mean of  $1.01^\circ \pm 0.01^\circ$ .

The independence of the mean pitch and mean roll values from wind and wave conditions (not shown) support the conclusion that the EASI yoke successfully decoupled EASI from the mooring forces, with the mean pitch angles resulting from the ballasting of

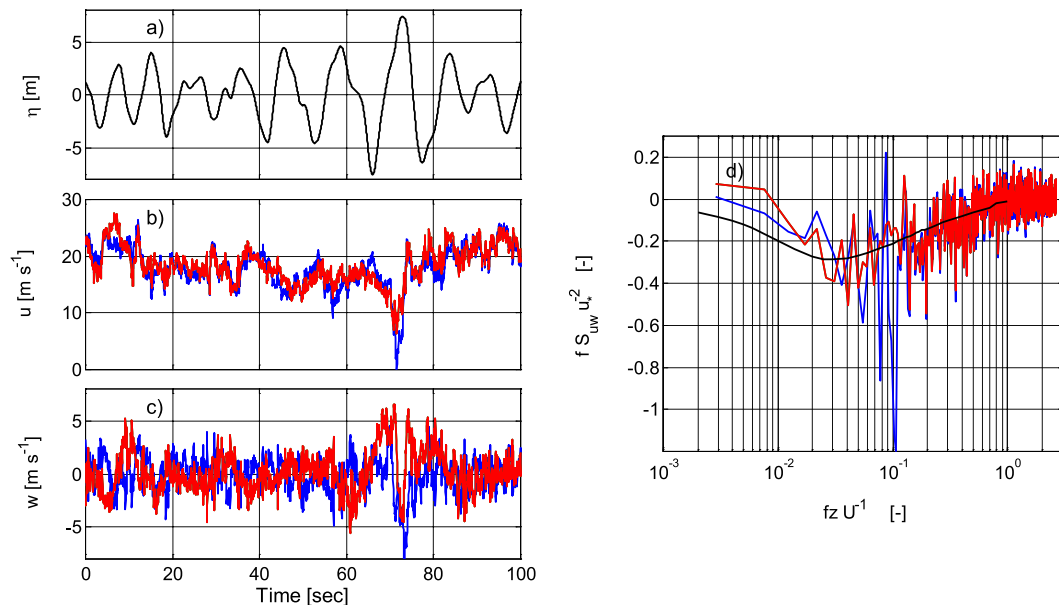


FIG. 8. Time series of (a) surface elevation, (b) horizontal wind (along-wind component), and (c) vertical wind. The blue lines show the signal as measured and the red lines after motion correction. (d) The 30-min cospectra of  $uw$  in dimensionless coordinates. Colors at left, with black representing the Miyake et al. (1970) universal curve,  $f$  is frequency,  $U$  is mean wind speed,  $z$  is the measurement height, and  $u_*$  is the friction velocity. Time series are from the same time as Fig. 5, during Typhoon Chaba. The cospectra include the same period.

EASI. We note that in contrast the ASIS platform mean tilt increases quadratically with wind speed and reached  $23^\circ$  during the almost  $20 \text{ m s}^{-1}$  wind speeds in the Southern Ocean (Sahlée et al. 2012). The error associated with nonzero pitch angle on SW radiation measurements is a function primarily of both pitch angle and sun azimuth angle (MacWhorter and Weller 1991). For solar azimuth angles under  $30^\circ$  ( $0^\circ$  being overhead), the  $5^\circ$  mean tilt results in an error in SW radiation of  $O(5\%)$  or less. This increases to 10% for solar azimuth angles over  $45^\circ$ . The platform rocking will increase this error in both cases. In future deployments, the trim of EASI in the water will be better accounted for in leveling the radiometers. This should significantly reduce the mean pitch angle of the radiometer and thence the error.

The air temperature plot (Fig. 3d) shows considerable noise at low winds. These data, from the Rotronic housed in the modified (partially sealed) R. M. Young shield, are clear evidence that the modified shield does not have sufficient ventilation at low winds. In these cases, temperature from other nearby, and well ventilated, sensors was used. However, at high winds, the Rotronics in the modified shields do not show signs of wetting, whereas those in the standard shields were compromised. It is clear that multiple sensors provide the highest chance of a continuous usable temperature dataset.

In summary, the Extreme Air–Sea Interaction buoy has proven to be a platform well suited for making quality wave and near-surface turbulence measurements (including air–sea fluxes) in high wind and wave conditions. Several manuscripts describing the data collected during ITOP have been submitted.

*Acknowledgments.* The development of EASI was funded by NSF-OCE-0526442, through the OTIC program. Our participation in ITOP was funded by ONR under Grant N0014-09-1-0392. We thank both agencies for their continued support. In addition we acknowledge the contributions of Mike Rebozo (RSMAS); Joe Gabriele and Cary Smith of Environment Canada; John Kemp and the WHOI mooring group; David Tang, Ruey-Chang Wei, Yiing Jang Yang, Yih Yang, and our TORI colleagues. We are grateful for the excellent support and assistance provided by the captains and crew of the R/V *Roger Revelle*. We thank an anonymous reviewer for prompting the discussion on rotation angle errors.

## REFERENCES

- Antclif, F., M. A. Donelan, W. M. Drennan, and H. C. Graber, 1994: Eddy correlation measurements of air–sea fluxes from a discus buoy. *J. Atmos. Oceanic Technol.*, **11**, 1144–1150, doi:10.1175/1520-0426(1994)011<1144:ECMOAS>2.0.CO;2.
- Andreas, E. L., 1992: Sea spray and turbulent air–sea fluxes. *J. Geophys. Res.*, **97**, 11 429–11 441, doi:10.1029/92JC00876.

- Banner, M. L., and W. K. Melville, 1976: On the separation of air flow over water waves. *J. Fluid Mech.*, **77**, 825–842, doi:[10.1017/S0022112076002905](https://doi.org/10.1017/S0022112076002905).
- Bao, J.-W., C. W. Fairall, S. A. Michelson, and L. Bianco, 2011: Parameterizations of sea-spray impact on the air–sea momentum and heat fluxes. *Mon. Wea. Rev.*, **139**, 3781–3797, doi:[10.1175/MWR-D-11-00007.1](https://doi.org/10.1175/MWR-D-11-00007.1).
- Belcher, S. E., and J. C. R. Hunt, 1998: Turbulent flow over hills and waves. *Annu. Rev. Fluid Mech.*, **30**, 507–538, doi:[10.1146/annurev.fluid.30.1.507](https://doi.org/10.1146/annurev.fluid.30.1.507).
- Bourassa, M. A., and Coauthors, 2013: High-latitude ocean and sea ice surface fluxes: Challenges for climate research. *Bull. Amer. Meteor. Soc.*, **94**, 403–423, doi:[10.1175/BAMS-D-11-00244.1](https://doi.org/10.1175/BAMS-D-11-00244.1).
- Donelan, M. A., 1990: Air-sea interaction. *Ocean Engineering Science*, B. LeMéhauté and D. Hanes, Eds., *The Sea*, Vol. 9, John Wiley and Sons, 239–292.
- , B. K. Haus, N. Reul, W. J. Plant, M. Stiassnie, H. C. Graber, O. B. Brown, and E. S. Saltzman, 2004: On the limiting aerodynamic roughness of the ocean in very strong winds. *Geophys. Res. Lett.*, **31**, L18306, doi:[10.1029/2004GL019460](https://doi.org/10.1029/2004GL019460).
- Drennan, W. M., 2006: On parameterisations of air-sea fluxes. *Atmosphere-Ocean Interactions*, W. Perrie, Ed., Vol. 2, WIT Press, 1–33.
- , and L. K. Shay, 2006: On the variability of the fluxes of momentum and sensible heat. *Bound.-Layer Meteor.*, **119**, 81–107, doi:[10.1007/s10546-005-9010-z](https://doi.org/10.1007/s10546-005-9010-z).
- , H. C. Graber, D. Hauser, and C. Quentin, 2003: On the wave age dependence of wind stress over pure wind seas. *J. Geophys. Res.*, **108**, 8062, doi:[10.1029/2000JC000715](https://doi.org/10.1029/2000JC000715).
- , J. A. Zhang, J. R. French, C. McCormick, and P. G. Black, 2007: Turbulent fluxes in the hurricane boundary layer. Part II: Latent heat fluxes. *J. Atmos. Sci.*, **64**, 1103–1115, doi:[10.1175/JAS3889.1](https://doi.org/10.1175/JAS3889.1).
- Dupuis, H., C. Guerin, D. Hauser, A. Weill, P. Nacass, W. Drennan, S. Cloché, and H. Graber, 2003: Impact of flow distortion corrections on turbulent fluxes estimated by the inertial dissipation method during the FETCH experiment on R/V *L'Atalante*. *J. Geophys. Res.*, **108**, 8064, doi:[10.1029/2001JC001075](https://doi.org/10.1029/2001JC001075).
- Eckman, R. M., R. J. Dobosy, D. L. Auble, T. W. Strong, and T. L. Crawford, 2007: A pressure-sphere anemometer for measuring turbulence and fluxes in hurricanes. *J. Atmos. Oceanic Technol.*, **24**, 994–1007, doi:[10.1175/JTECH2025.1](https://doi.org/10.1175/JTECH2025.1).
- Edson, J. B., A. A. Hinton, K. E. Prada, J. E. Hare, and C. W. Fairall, 1998: Direct covariance flux estimates from mobile platforms at sea. *J. Atmos. Oceanic Technol.*, **15**, 547–562, doi:[10.1175/1520-0426\(1998\)015<0547:DCFEFM>2.0.CO;2](https://doi.org/10.1175/1520-0426(1998)015<0547:DCFEFM>2.0.CO;2).
- Fairall, C. W., and Coauthors, 2009: Observations to quantify air-sea fluxes and their role in climate variability and predictability. *Proceedings of OceanObs'09: Sustained Ocean Observations and Information for Society*, J. Hall, D. E. Harrison, and D. Stammer, Eds., Vol. 2, ESA Publ. WPP-306, doi:[10.5270/OceanObs09.cwp.27](https://doi.org/10.5270/OceanObs09.cwp.27).
- French, J. R., W. M. Drennan, J. A. Zhang, and P. G. Black, 2007: Turbulent fluxes in the hurricane boundary layer. Part I: Momentum flux. *J. Atmos. Sci.*, **64**, 1089–1102, doi:[10.1175/JAS3887.1](https://doi.org/10.1175/JAS3887.1).
- Gemmrich, J. R., and D. M. Farmer, 2004: Near-surface turbulence in the presence of breaking waves. *J. Phys. Oceanogr.*, **34**, 1067–1086, doi:[10.1175/1520-0485\(2004\)034<1067:NTITPO>2.0.CO;2](https://doi.org/10.1175/1520-0485(2004)034<1067:NTITPO>2.0.CO;2).
- Graber, H. C., E. A. Terray, M. A. Donelan, W. M. Drennan, J. C. Van Leer, and D. B. Peters, 2000: ASIS—A new air-sea interaction spar buoy: design and performance at sea. *J. Atmos. Oceanic Technol.*, **17**, 708–720, doi:[10.1175/1520-0426\(2000\)017<0708:AANASI>2.0.CO;2](https://doi.org/10.1175/1520-0426(2000)017<0708:AANASI>2.0.CO;2).
- Katsaros, K. B., and J. E. Devault, 1986: On irradiance measurement errors at sea due to tilt of pyranometers. *J. Atmos. Oceanic Technol.*, **3**, 740–745, doi:[10.1175/1520-0426\(1986\)003<0740:OIMEAS>2.0.CO;2](https://doi.org/10.1175/1520-0426(1986)003<0740:OIMEAS>2.0.CO;2).
- , M. A. Donelan, and W. M. Drennan, 1993: Flux measurements from a SWATH ship in SWADE. *J. Mar. Syst.*, **4**, 117–132, doi:[10.1016/0924-7963\(93\)90003-5](https://doi.org/10.1016/0924-7963(93)90003-5).
- Knobles, D. P., S. M. Joshi, R. D. Gaul, H. C. Graber, and N. J. Williams, 2008: Analysis of wind-driven ambient noise in a shallow water environment with a sandy seabed. *J. Acoust. Soc. Amer.*, **124**, EL157–EL162, doi:[10.1121/1.2960976](https://doi.org/10.1121/1.2960976).
- Longuet-Higgins, M. S., 1985: Accelerations in steep gravity waves. *J. Phys. Oceanogr.*, **15**, 1570–1579, doi:[10.1175/1520-0485\(1985\)015<1570:AISGW>2.0.CO;2](https://doi.org/10.1175/1520-0485(1985)015<1570:AISGW>2.0.CO;2).
- MacWhorter, M. A., and R. A. Weller, 1991: Error in measurements of incoming shortwave radiation made from ships and buoys. *J. Atmos. Oceanic Technol.*, **8**, 108–117, doi:[10.1175/1520-0426\(1991\)008<0108:EIMOIS>2.0.CO;2](https://doi.org/10.1175/1520-0426(1991)008<0108:EIMOIS>2.0.CO;2).
- Mahrt, L., D. Vickers, W. M. Drennan, H. C. Graber, and T. L. Crawford, 2005: Displacement measurement errors from moving platforms. *J. Atmos. Oceanic Technol.*, **22**, 860–868, doi:[10.1175/JTECH1727.1](https://doi.org/10.1175/JTECH1727.1).
- Makin, V. K., 1998: Air-sea exchange of heat in the presence of wind waves and spray. *J. Geophys. Res.*, **103**, 1137–1152, doi:[10.1029/97JC02908](https://doi.org/10.1029/97JC02908).
- Miyake, M., R. W. Stewart, and R. W. Burling, 1970: Spectra and spectra of turbulence over water. *Quart. J. Roy. Meteor. Soc.*, **96**, 138–143, doi:[10.1002/qj.49709640714](https://doi.org/10.1002/qj.49709640714).
- Norris, S. J., I. M. Brooks, G. de Leeuw, M. H. Smith, M. Moerman, and J. J. N. Lingard, 2008: Eddy covariance measurements of sea spray particles over the Atlantic Ocean. *Atmos. Chem. Phys.*, **8**, 555–563, doi:[10.5194/acp-8-555-2008](https://doi.org/10.5194/acp-8-555-2008).
- Oost, W. A., C. W. Fairall, J. B. Edson, S. D. Smith, R. J. Anderson, J. A. B. Wills, K. B. Katsaros, and J. DeCosmo, 1994: Flow distortion calculations and their application in HEXMAX. *J. Atmos. Oceanic Technol.*, **11**, 366–386, doi:[10.1175/1520-0426\(1994\)011<0366:FDCATA>2.0.CO;2](https://doi.org/10.1175/1520-0426(1994)011<0366:FDCATA>2.0.CO;2).
- Pederos, R., G. Dardier, H. Dupuis, H. C. Graber, W. M. Drennan, A. Weill, C. Guérin, and P. Nacass, 2003: Momentum and heat fluxes via the eddy correlation method on the R/V *L'Atalante* and an ASIS buoy. *J. Geophys. Res.*, **108**, 3339, doi:[10.1029/2002JC001449](https://doi.org/10.1029/2002JC001449).
- Pettersson, H., H. C. Graber, D. Hauser, C. Quentin, K. K. Kahma, W. M. Drennan, and M. A. Donelan, 2003: Directional wave measurements from three wave sensors during the FETCH experiment. *J. Geophys. Res.*, **108**, 8061, doi:[10.1029/2001JC001164](https://doi.org/10.1029/2001JC001164).
- Powell, M. D., P. J. Vickery, and T. A. Reinhold, 2003: Reduced drag coefficient for high wind speeds in tropical cyclones. *Nature*, **422**, 279–283, doi:[10.1038/nature01481](https://doi.org/10.1038/nature01481).
- Pun, I. F., Y.-T. Chang, I.-I. Lin, T. Y. Tang, and R.-C. Lien, 2011: Typhoon-ocean interaction in the western North Pacific: Part 2. *Oceanography*, **24**, 32–41, doi:[10.5670/oceanog.2011.92](https://doi.org/10.5670/oceanog.2011.92).
- Reul, N., H. Branger, and J. P. Giovanangeli, 1999: Air flow separation over unsteady breaking waves. *Phys. Fluids*, **11**, 1959–1961, doi:[10.1063/1.870058](https://doi.org/10.1063/1.870058).
- Sahlée, E., and W. M. Drennan, 2009: Measurements of damping of temperature fluctuations in a tube. *Bound.-Layer Meteor.*, **132**, 339–348, doi:[10.1007/s10546-009-9396-0](https://doi.org/10.1007/s10546-009-9396-0).

- , ——, H. Potter, and M. A. Rebozo, 2012: Waves and air-sea fluxes from a drifting ASIS buoy during the Southern Ocean Gas Exchange Experiment. *J. Geophys. Res.*, **117**, C08003, doi:[10.1029/2012JC008032](https://doi.org/10.1029/2012JC008032).
- Smith, S. D., 1980: Wind stress and heat flux over the ocean in gale force winds. *J. Phys. Oceanogr.*, **10**, 709–726, doi:[10.1175/1520-0485\(1980\)010<0709:WSAHFO>2.0.CO;2](https://doi.org/10.1175/1520-0485(1980)010<0709:WSAHFO>2.0.CO;2).
- Terray, E. A., M. A. Donelan, Y. C. Agrawal, W. M. Drennan, K. K. Kahma, A. J. Williams III, P. A. Hwang, and S. A. Kitaigorodskii, 1996: Estimates of kinetic energy dissipation under breaking waves. *J. Phys. Oceanogr.*, **26**, 792–807, doi:[10.1175/1520-0485\(1996\)026<0792:EOKEDU>2.0.CO;2](https://doi.org/10.1175/1520-0485(1996)026<0792:EOKEDU>2.0.CO;2).
- Timpe, G. L., and N. van de Voorde, 1995: NOMAD buoys: An overview of forty years of use. *OCEANS '95 MTS/IEEE: Challenges of Our Changing Global Environment*, Vol. 1, IEEE, 309–315, doi:[10.1109/OCEANS.1995.526788](https://doi.org/10.1109/OCEANS.1995.526788).
- Zhang, J. A., 2010: Spectral characteristics of turbulence in the hurricane boundary layer over the ocean between the outer rain bands. *Quart. J. Roy. Meteor. Soc.*, **136**, 918–926, doi:[10.1002/qj.610](https://doi.org/10.1002/qj.610).